Brightest Cluster Galaxies in Strongly-Lensing Galaxy Clusters and Richness- and Redshift-Matched Samples

A thesis submitted in partial fulfillment of the requirements for the degree of
Bachelor of Science in Astrophysics with Honors

Benjamin Levine
Advisor: Professor Michael Gladders

ABSTRACT

We present a statistical analysis of 588 strongly-lensing galaxy clusters and groups, selected from publicly-available imaging sky surveys primarily by the COOL-LAMPS (ChicagO Optically selected strong Lenses — Located At the Margins of Public Surveys) collaboration. The foreground lenses are found at photometric redshifts $0.2 < z < 1.2$. Using photometric methods, we compare this extensive sample of hundreds of strong-lensing systems to a sample of non-lensing systems that are matched in redshift and galaxy richness. Previous work on SDSS data has suggested that the luminosity of a cluster's brightest cluster galaxy (BCG) may be related to its lensing potential, in that lensing BCGs are significantly brighter than non-lensing counterparts in an otherwise matched sample. We independently confirm this trend using DECaLS data and a custom redshift- and richness-estimation pipeline, and find that lensing BCGs tend to have a 27.0% larger half-light radius than non-lensing BCGs. We additionally find that lensing clusters tend to be more centrally concentrated in projection along the line-of-sight than non-lensing clusters matched in larger richness apertures. This effect is unlikely to be caused by cluster orientation bias alone. We find no evidence of ellipticity differences in the sample BCGs, but do find marginally-significant differences in positions of the BCGs versus the second brightest cluster members.

1. INTRODUCTION

1.1. *Overview and Motivation*

The increasing scale, scope, and depth of cosmic surveys has introduced new opportunities for discovering and studying gravitational lensing. Lensing, an effect of general relativity, causes light rays from a distant object to be bent by an intervening mass, resulting in measurable changes to the shape and magnitude of the resulting image. In the most extreme cases — dubbed strong lensing — multiple images of the background source may be visible, magnified by several orders of magnitude and thus presenting an exciting opportunity to study these lensed sources in great detail. Studying the nature of the lensing effect also allows for modeling the mass structure of the intervening object, which is dominated by dark matter at group and cluster scales. This information is of significance to cosmology, as the behavior of galaxy clusters and their dark matter halos is an important test of the evolution of structure in the universe.

Strong gravitational lensing is rare and has historically been difficult to find; however, the abundance of data from large cosmic surveys such as the Dark Energy Camera Legacy Survey (DECaLS; Dey et al. 2019; Schlegel et al. 2021) presents a way to quickly and efficiently detect strong lensing, as well as access photometric information without the need for follow-up imaging. Previous work has employed both visual identification (e.g., Khullar et al. 2021) and machine learning algorithms (e.g., Huang et al. 2020) to find hundreds of new lensing systems in DECaLS. This progress provides a large sample of lenses with high statistical significance, critical for studying the properties of lenses and lensing systems.

Whether the number and properties of strong lenses discovered so far is in tension with the expectations of current cosmological models remains an open question (e.g., Bartelmann et al. 1998; Gladders et al. 2003; Meneghetti et al. 2011, 2020). Previous work has suggested that the luminosity of a cluster's brightest cluster galaxy (BCG) may be related to its lensing potential, and that lensing BCGs are significantly brighter than non-lensing counterparts in a redshift- and richness- matched sample (Stephan 2014). Exploring this discrepancy will improve our understanding of large-scale structure and cluster formation in the universe, as well as dark matter distribution in massive clusters.

1.2. *Strong Gravitational Lensing*

Einstein's general theory of relativity characterizes spacetime by its curvature, a property which is determined by the mass distribution throughout a given space. The theory also requires that light must travel along so-called "null geodesics," which follow the shortest paths between two points through the curved spacetime geometry. In flat space, these photon paths radiate symmetrically from a source object, and there is only one shortest path that connects any two points (i.e. a straight line). However, in a curved spacetime there may be multiple null geodesics, resulting in more than one possible photon path between two objects. This effect is known as strong gravitational lensing, and takes the form of either duplicate images or large, distorted "arcs."

In the thin lens approximation, lensing is described in terms of photon deflection angles at the mass plane — that is, how far a ray of light is deflected from its flat-space straight path by a mass. According to general relativity, the deflection angle of light α due to a point mass is

$$\alpha = \frac{4GM}{c^2 b} \equiv \frac{2R_S}{b} \tag{1}$$

where M is the deflecting mass, b is the impact parameter, R_S is the Schwarzschild radius, and $\frac{M}{b}$ is small. The deflection angle in a gravitational lens is illustrated in Figure 1.

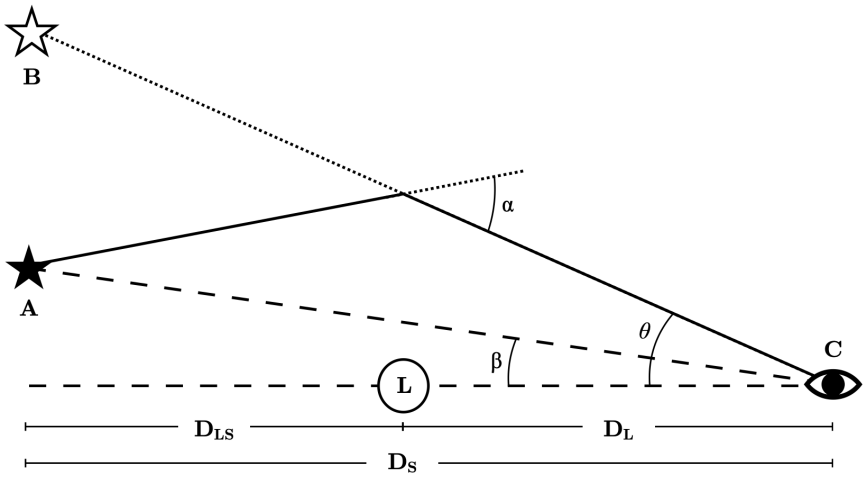

Figure 1. An illustration of gravitational lensing by a point mass at L. Light rays emitted from source at A will follow solid lines, but an observer at C will observe an image of the source at B. The deflection angle, α, is angular difference between the light ray's emitted trajectory and its lensed trajectory. Adapted from Hartle (2003).

Using trigonometry, one can compute the Lens Equation:

$$\theta D_S = \beta D_S + \alpha D_{LS} \tag{2}$$

which may also be written as

$$\theta = \beta + \frac{\theta_E^2}{\theta} \tag{3}$$

where the Einstein angle, θ_E, is given by

$$\theta_E = \left[2R_S \left(\frac{D_{LS}}{D_S D_L} \right) \right]^{1/2} \tag{4}$$

The Einstein angle is the angular distance between the lensing mass and the observed image when the impact parameter is 0 — that is, when the observed object is directly behind the lensing mass. Since observable lenses generally have $\beta \ll \theta$, the Einstein

angle is a characteristic parameter for most lenses, and it allows for simple modeling of lensing behavior using only θ, D_S, D_L, D_{LS}, and the lensing mass.

In addition to changing the image position and producing multiple images, lensing also affects observed flux. This is of great significance to astronomy because apparent magnitude is a limiting factor for telescopes.

In general, the lensing magnification is a function of the radial width and tangential extent of the lensed arc. This is given by solving the Lens Equation (Equation 3) to find the radius for an arc with angular offset β:

$$\theta_{\pm} = \frac{1}{2}\left[\beta \pm \left(\beta^2 + 4\theta_E^2\right)^{1/2}\right] \tag{5}$$

and then differentiating to obtain

$$\Delta\theta_{\pm} = \frac{\Delta\beta}{2}\left[1 \pm \beta\left(\beta^2 + 4\theta_E^2\right)^{-1/2}\right] \tag{6}$$

where $\Delta\theta$ is the radial angular size of the image and $\Delta\beta$ is the radial angular size of the source. Assuming the source radiates uniformly from all parts of its surface, the observed flux must then be directly proportional to the size of the lensed image. The magnification is thus

$$\frac{B_{\pm}}{B_0} = \frac{\Delta\Omega_{\pm}}{\Delta\Omega_0} = \left|\frac{\theta_{\pm}\Delta\theta_{\pm}\Delta\phi}{\beta\Delta\beta\Delta\phi}\right| \tag{7}$$

in which $B_{\pm}$ is the lensed brightness, B_0 is the source brightness, $\Delta\Omega$ is the solid angle, and ϕ is the angular length of the lensed arc. ϕ is conserved, as the angular length of the arc does not change, so the equation simplifies to

$$\frac{B_{\pm}}{B_0} = \frac{1}{4}\left[\beta\left(\beta^2 + 4\theta_E^2\right)^{-1/2} + \beta^{-1}\left(\beta^2 + 4\theta_E^2\right)^{1/2} \pm 2\right] \tag{8}$$

$\frac{B_+}{B_0} \geq 1$ for all positive values of β, so the outer lensed image will always be brighter than the source. This magnification can be extreme when β is small and θ_E is large. This means that the most magnified examples of lensing occur when the source is almost perfectly aligned with the lens, and the lens is massive. However, in order for the magnification to be significant without θ_E being unreasonably large, β must be extremely small. This means that almost all strong lensing requires precise alignment between the lensed object and the lensing mass.

1.3. *Galaxy Clusters*

Matter in the universe is not uniformly distributed. Galaxies, their surrounding intergalactic matter, and dark matter halos are clustered together with a density distribution characterized by the matter power spectrum (Schuecker et al. 2001). According to ΛCDM theories of cosmology, these overdensities have their origins in early density fluctuations of dark matter, seeded by quantum fluctuations from the inflationary epoch. These fluctuations, uncoupled from photons at all times, grew due to gravity in the early universe, and the collapse of baryonic matter in these overdensities eventually formed the large, gravitationally-bound groups of galaxies

which trace the observed structure of the universe today. Thus, observed matter distributions in clusters — including the direct measure of mass distributions (dark or otherwise) observed via strong lensing — are a important measurement of dark matter in cosmological models (e.g., Bocquet et al. 2019)

Particularly massive groups of galaxies are known as galaxy clusters. Large clusters are typically distinguished by a luminous brightest cluster galaxy (BCG), accompanied by various satellite galaxies occupying the same cluster-scale dark matter halo. These BCGs are thought to be formed through mergers (Dubinski 1998), meaning that their stars are thought to have a more complex history than a typical giant elliptical in a massive cluster.

Clusters are classified by their richness λ: the number of galaxies that are gravitationally bound together. Unfortunately, this quantity is not easily measured because it can be difficult to distinguish between true cluster members and nearby non-members in either the foreground or background of the cluster, and the radial extent of a cluster is often unclear. Various methods have been used to estimate richness. Abell (1958) defined richness as the number of galaxies within 2 magnitudes of the third-brightest galaxy, in an area of approximately 3 Mpc, while Bahcall (1981) used the same strategy with a radius of 0.5 Mpc. Abell et al. (1989) defined a radius based on the magnitude of the tenth-brightest galaxy. Yee & López-Cruz (1999) modeled a cluster luminosity function and spatial profile, and compared these with total galaxy counts to estimate a richness. Rykoff et al. (2014), in developing REDMAPPER — one of the most recent cluster analysis algorithms (and the calibration sample for this work) — estimated richness by computing the likelihood that any given galaxy is a member of the cluster, based on its observable properties, the cluster density profile, and the background galaxy density.

In this work, our goal is not to compute exact, mass-calibrated richness values for the purpose of, for instance, constraining cosmological parameters. Rather, we aim to use richnesses to simply select corresponding samples of lensing and non-lensing clusters at matched redshifts. Since all our clusters are drawn from the same fundamental data, small biases in our richness algorithm should be consistent between samples. Therefore, our algorithm counts galaxies within a predefined radius, with a simple background correction, because it maintains good accuracy while also being computationally straightforward and efficient.

1.4. *Rarity of Strong Lenses*

Due to the required alignment between a lensed object and its lensing mass, strong lenses are extremely rare. In addition, the lensing mass must be sufficiently large to produce a magnified image, and D_L and D_{LS} must be correctly spaced so that θ_E is large. Galaxy clusters satisfy some of these problems: they can have large masses and are found at sufficient distances to produce large θ_E. However, massive clusters are rare, and it is even less likely for one to be aligned with a background object.

Despite this, some early studies have suggested that strong, cluster-scale lenses occur at a rate higher than would be expected given the current understanding of cosmology. Bartelmann et al. (1998) used cluster simulations to test cluster lensing potential in

various cosmological models, finding that ΛCDM predicts an order of magnitude fewer lenses than observed. Gladders et al. (2003) confirmed this disagreement using a different cluster sample, and suggested that the solution may lie in the properties of the lenses themselves. Other, more recent work, instead finds no difference between predicted and observed lens frequency. There has been much work on this topic in recent decades; for a review of this field, see Meneghetti et al. (2013). There continue to be discrepancies found in the most modern work, such as Meneghetti et al. (2020) which claims order-of-magnitude overabundances in lensing substructures as compared to simulations of 11 clusters.

The disagreements in this field generate a motivation for studying the properties and statistics of lensing clusters. Information about why individual clusters are efficient lenses may be flagged by physical parameters such as luminosity, ellipticity, or substructure. This conclusion is supported by Stephan (2014), who found that BCGs in a sample of 50 lensing clusters were more luminous than BCGs in a corresponding sample of non-lensing clusters. The luminosity of the BCG may be an effect of deeper structural properties which influence the lensing cross section.

We aim to reproduce this result in a more extensive sample, and to broadly examine physical properties of lensing BCGs and clusters. This work aims to provide insights into the nature of lensing cluster cross sections and the dark matter structure of galaxy clusters, and additionally will inform future strong lensing searches.

2. LENSING SAMPLE SELECTION

This work utilizes discoveries of lensed systems made by the COOL-LAMPS project, a collaboration designed as the focus of an undergraduate research class at the University of Chicago. COOL-LAMPS visually searches survey footprints to identify strong lensing candidates, and to date has found over 600 cluster- and group-scale strong lens candidates in the DECaLS footprint (as well as many more lenses on smaller scales). We use 600 such systems here, all of which are sufficiently obvious in the DECaLS images that we drop the qualifier "candidate" from further description of the sample. A set of example systems is shown in Figure 2. While a main focus of the COOL-LAMPS project is to perform follow-up observations on photometrically-distinct lensed galaxies, this large sample also provides a unique and powerful opportunity to study population statistics of the lenses themselves.

The COOL-LAMPS lens search method is as follows. Candidate lines-of-sight are selected by finding luminous red galaxies with de Vaucouleurs profiles (de Vaucouleurs 1948). The galaxies are selected based on a color-magnitude cut such that they are brighter and redder than a passively-evolving galaxy, of a notional mass, formed at redshift 3. DECaLS *grz* images are constructed and displayed individually (for the richest potential lenses) through groupings of up to 15 lines-of-sight at once (for potentials that appear to be isolated individual galaxies). The individual cutouts range from 30 to 90 arcseconds square, depending on the apparent system richness. The mass cut (and hence observed apparent magnitude cut) is tuned primarily to result in a reasonable number of lines of sight to be searched; however, comparison in overlapping areas with the (SDSS; York et al. 2000; Blanton et al. 2017) and

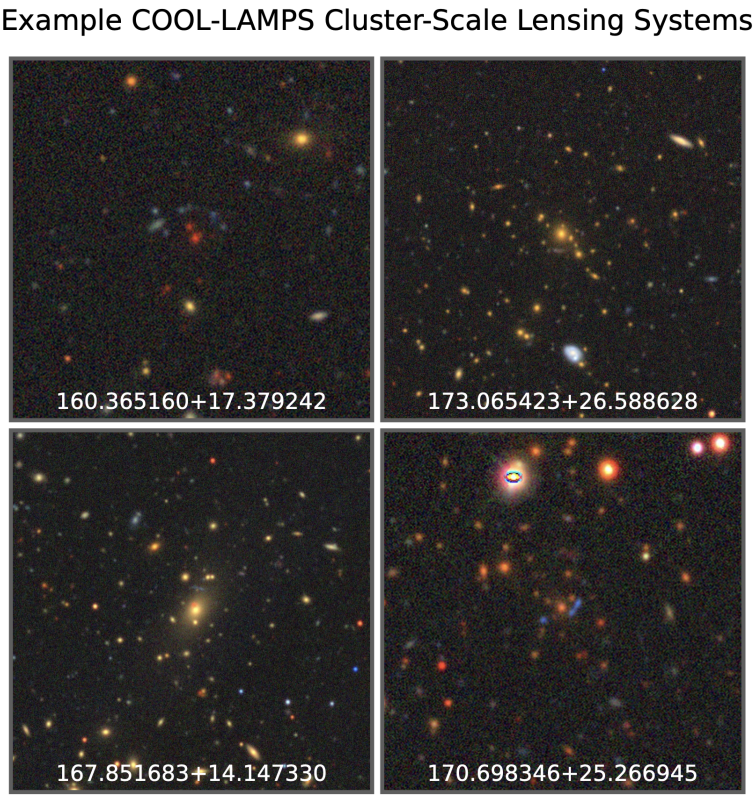

Figure 2. Four examples of cluster-scale lenses from the COOL-LAMPS sample. RA+Dec positions are noted for each cluster in degrees.

older Sloan Giant Arcs Survey (SGAS; Hennawi et al. 2008) results shows that this cut captures more than 95% of SGAS lenses, which were selected from a group and cluster catalog. Each group is viewed by an examiner using a custom-built Python ranking tool, and given an integer score between 0 and 3 based on the evidence for lensing in one or more of the images. A minimum of three examiners score each image; lines of sight with high aggregate scores are chosen for follow-up study.

As mentioned above, the COOL-LAMPS analysis of the DECaLS footprint overlaps with much of the SDSS area. We presume that many previously-discovered cluster-scale lenses in SDSS, such as those in SGAS, will be included in our sample. We have not, however, attempted to use machine learning-based samples of lenses (e.g., Huang et al. 2020), as our current understanding is that such catalogs tend to be comprised of mostly galaxy-scale lenses, rather than cluster-scale.

3. CONSTRUCTING A MATCHED CLUSTER SAMPLE

We aim to select a sample of DECaLS non-lensing clusters that are matched to our lensing sample in both redshift and richness. Measuring cluster richness and redshift is a well established process in the SDSS data (e.g., Koester et al. 2007; Rykoff et al. 2014) based on variations of red-sequence cluster selections methods (Gladders & Yee 2000).

However, the DECaLS photometry is significantly deeper, and therefore pushes to higher redshifts, than published cluster catalogs based on data from the SDSS. In

addition, we aim to measure richness in arbitrarily-sized apertures in order to explore the differences in BCGs between lensing and non-lensing clusters matched in richness at a range of radial scales. To satisfy these requirements, we construct a cluster analysis algorithm tailored to DECaLS data that is capable of calculating a range of redshifts (up to $z = 1.5$) and estimating richnesses at any given aperture scale.

3.1. *Redshift Calculation*

The calculation of redshift and richness begins with the former, as the richness measurement is based on the number of galaxies at a given redshift range within the designated aperture. We therefore begin by developing a simple method to estimate the photometric redshift of any given red-sequence object.

Our algorithm takes advantage of the red-sequence color-magnitude relation, first noted by Baum (1959), established as a universal linear relation with small scatter by Bower et al. (1992), and since used extensively as a tool for finding and characterizing galaxy clusters and groups (e.g., Gladders & Yee 2000). For any given redshift slice, we expect all red-sequence galaxies to lie on a linear locus within the color-magnitude space for all color filters, with the strongest color differentiation with redshift occurring for filter pairs that span the observed 4000Å break. Since galaxy clusters are chiefly comprised of red-sequence galaxies, we can use this relationship to fit the redshift for any galaxy in the cluster.

Our input description of the red sequence model is constructed based on photometric observations from the DECaLS Data Release 8 catalog, combined with overlapping galaxy redshifts from the SDSS. Specifically, we use the spectroscopic redshifts from SDSS Data Release 16. We extract all photometric objects from the DECaLS catalogs that are characterized with a de Vaucouleurs profile, within a projected distance of 0.5 Mpc of each spectroscopic object in a narrow redshift bin. These galaxies are likely to be at the same redshift because galaxies — especially those that lie on the red sequence — are clustered in three dimensions, meaning that galaxies nearby an object at known z are likely to lie at the same z. The ridge-line of red-sequence galaxies in the composite color-magnitude diagram of these objects is then fit with a line, yielding a description of the red-sequence at that redshift. Figure 3 shows an example of this resulting color-magnitude diagram and fit.

To extend this model to redshifts beyond that which the SDSS data samples well, we then fit the measured red-sequences with a simple photometric model consisting of two evolutionary tracks for a $z = 3$ instantaneous burst model of an early-type galaxy, sampled at metallicities of 1.0 and 0.4 of solar. We find the luminosity of each track such that a line connecting the two in observed color-magnitude space best fits the measured red-sequences, and the predicted red-sequence properties of this synthetic photometry are used to extend the red sequence model to higher redshifts.

To fit data to this model, we select the redshift bin that is nearest to the data in color-magnitude space, as visualized in Figure 3. We compute one redshift for the *gr*-*r* space and one for the *rz*-*z* space. We combine these predictions into a final redshift in one of three ways:

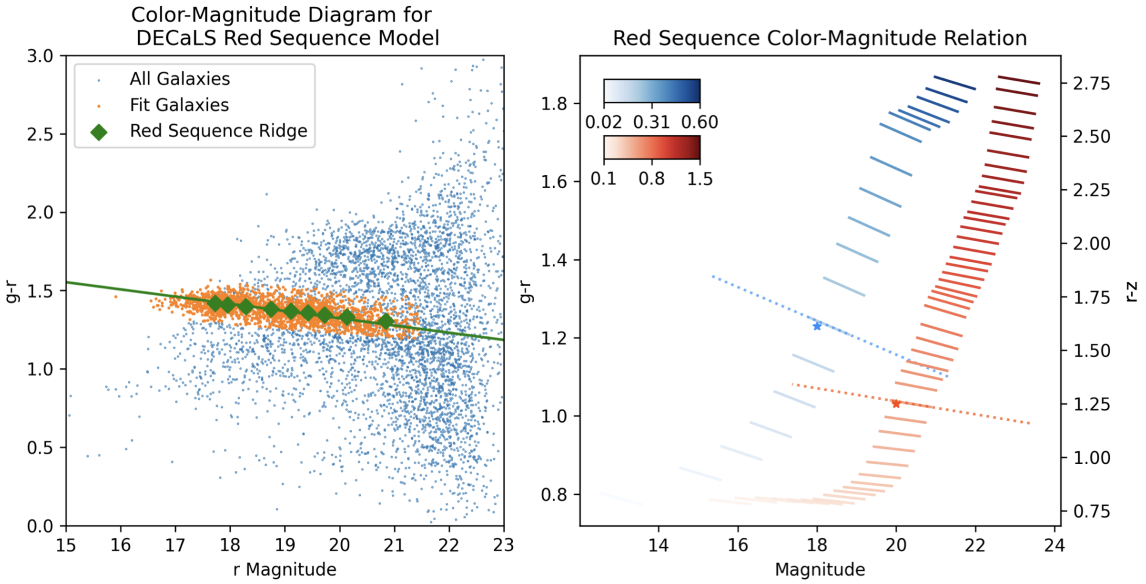

Figure 3. Left: A color-magnitude diagram for DECaLS galaxies with de Vaucouleurs profiles, within 0.5Mpc and Δz=0.005 of spectroscopically confirmed SDSS galaxies at z=0.25. One out of every ten galaxies fitting this description is plotted. A line describing the red-sequence is fit to the galaxies colored orange, which are isolated from the broader distribution via iterated clipping. The green diamonds show a measurement of peak galaxy density in color, in ten magnitude bins of equal galaxy number. Right: The Red-Sequence Color-Magnitude relation model we use in our photometric redshift algorithm. The blue lines correspond to galaxies in the *gr* band, while red lines correspond to the *rz* band. The intensity of the color corresponds to redshift. For visual clarity, the number of lines shown is reduced by a factor of 300 compared to the model used in the algorithm. An example data point is plotted for an object with $r = 18; z = 20; g - r = 1.23; r - z = 1.25$.

$$z_{combined} \equiv Z_f(z_{gr}, z_{rz}) = \begin{cases} z_{gr} & \text{if } z_{gr} < 0.35. \\ z_{rz} & \text{if } z_{gr} > 0.60 \text{ or } z_{rz} > 0.40. \\ \frac{z_{gr}+z_{rz}}{2} & \text{otherwise.} \end{cases} \quad (9)$$

The first two categories are not mutually exclusive, and we give preference to the second combination (that is, if a galaxy has $z_{gr} < 0.35$ and $z_{rz} > 0.40$, we assign it $z = z_{rz}$).

Before beginning the calculation, we trim several classes of object from our data. First, we remove objects with DECaLS bitmasks 1 and 9, corresponding to the object touching a pixel within half of the locus of a radius-magnitude relation; and touching a pixel in a WISEMASK_W2 bright star mask. In testing, we found that these objects typically have high uncertainties or incorrect photometry that interfere in particular with the BCG identification process (see 3.2). Next, we remove all but the objects with DECaLS morphology profiles de Vaucouleurs (DEV), Sérsic (SER), Exponential (EXP), and Round Exponential (REX), which eliminates stars and other point sources from the catalog. Finally, we remove all objects with a magnitude $m > m_* - 2$, with m_* given by our redshift model, which eliminates faint sources

from consideration and ensures that the same absolute magnitude range is considered across all redshifts up to the completeness limit of the catalog.

Redshift error is estimated by propagating the photometric uncertainties in the DECaLS catalog, along with an additional uncertainty of 0.03 magnitudes added in quadrature to the photometric uncertainties to reflect a minimum floor to the intrinsic color scatter of galaxies on the red-sequence (Valentinuzzi et al. 2011).

In testing against known spectroscopic redshifts from SDSS, our results are linearly-correlated, but there is a discrepancy between the $g-r$ and $r-z$ redshift predictions (corresponding to redshifts $z < 0.35$ and $z > 0.4$ respectively). Our $g-r$ model tends to slightly underestimate redshift, while our $r-z$ model tends to overestimate redshift. Furthermore, the $g-r$ offset is correlated with our richness measurement (see Section 3.2), with lower richness clusters having larger redshift offsets. These offsets appear in comparison to both the SDSS spectroscopic redshift catalog and the DECaLS photometric redshift catalog (Zhou et al. 2021).

To address this issue, we compute the measured offset against the SDSS spectroscopic measurements (as well as the DECaLS photometric measurements at high redshifts where spectroscopic data is not available). For $r-z$ redshifts, which are not richness-dependent, we perform a linear fit of form $\delta = az + b$, where δ is the offset from the spectroscopic redshift. For $g-r$ redshifts, we first perform a polynomial fit of form $\delta_1 = a + b\lambda + c\lambda^2 + d\lambda^3 + e\lambda^4$; and then perform a second linear fit of form $\delta_2 = a\delta_1 + b$. Lastly, we compute a linear correction to the combined redshift distribution. Since the distribution of offsets in each redshift or richness bin is not necessarily normal, we pre-process our data by fitting a gaussian to the offset peak and ignoring any offsets beyond 3 standard deviations.

The algorithm is first run on the initial redshift prediction to produce an initial set of richnesses. These initial richnesses are used to correct the initial redshift, and the richnesses are finally recalculated with the corrected redshifts. The results of the correction are shown in Figure 4. In total, our redshift correction takes the form:

$$z_{combined} = f_1\Big(Z_f\big(f_2(z_{gr}, \lambda_{gr}), f_3(z_{rz})\big)\Big) \tag{10}$$

where f_n is a redshift correction function.

Compared to SDSS spectroscopic redshifts, our photometric results have a normally-distributed offset with a mean of 0.0004, and a standard deviation of 0.022. The deviations are on the same order of magnitude as redMaPPer , which has a mean offset of 0.0021 and a standard deviation of 0.018 when compared to the same sample; and superior to the DECaLS photometric catalog (Zhou et al. 2021), which has a mean offset of -0.0225 and a standard deviation of 1.505. In general, our estimator performs at similar accuracy to other modern photometric redshift algorithms. Since this study is comparative in nature, our results will be robust to any remaining biases in the redshift estimator (possibly occuring at high redshifts where there is minimal spectroscopic data to confine the red sequence model).

While the redshift model is generally robust, its implementation over catalog data may yield unexpected results for certain objects. DECaLS galaxies that are fitted

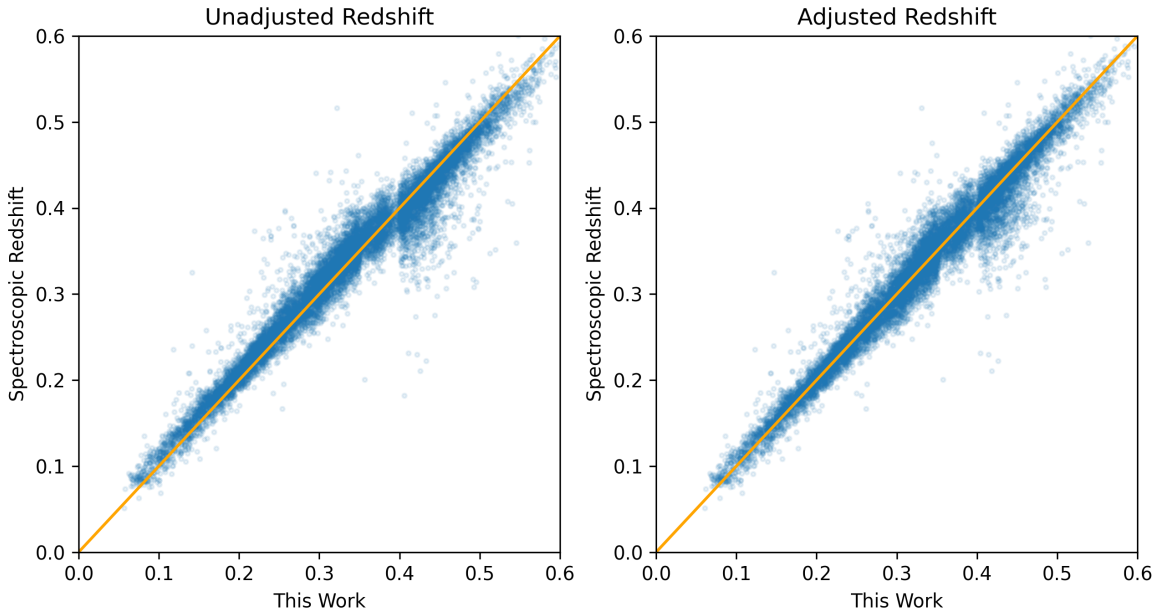

Figure 4. The unadjusted (left) and adjusted (right) redshift for spectroscopically-confirmed objects in the REDMAPPER catalog compared to our algorithm. In the unadjusted data, we tend to underestimate low redshifts and overestimate high redshifts. By comparison, our adjusted algorithm is centered on the spectroscopic results while being robust against tails in the distribution of offsets.

poorly (due to partial masking by a bright object, bad photometry, unusual shape, or another issue) may not have meaningful data in one or more filters. In this case, our redshift algorithm may not have z_{gr} or z_{rz} to compare, leading to less accurate predictions. For example, if a galaxy has $z_{gr} = 0.4$ and $z_{rz} = 0.5$, it should be assigned $z = z_{rz} = 0.5$. However, if the galaxy has bad z-band data, it will instead be assigned $z = z_{gr} = 0.4$. While uncommon, photometric issues such as these may result in true cluster members being missed, or non-cluster members being misclassified as part of the cluster. In addition, since bad data is not randomly distributed (photometric errors may often be clustered around a bright object), these redshift estimation errors may compound in single clusters.

3.2. *Richness Calculation*

The algorithm is designed to compute redshift and richness surrounding a galaxy pre-selected as a luminous red galaxy, and a likely location for strong lensing. However, given the nature of the selection process and catalog measurements, it is not guaranteed that the selected galaxy is the cluster BCG — instead, it may be a secondary massive galaxy, or part of a sub-structure within the cluster. Therefore, we begin by identifying the cluster BCG.

Given an arbitrary line of sight to a luminous red galaxy, the algorithm computes the redshift of the selected galaxy and then iteratively selects the brightest galaxy within a pre-defined distance and redshift range. A maximum limit of 100 iterations is set, although in practice this limit should rarely (if ever) be reached. The brightest galaxy is identified as the BCG, and the entire cluster algorithm is centered on its coordinates.

It is in principle possible for this algorithm to wander to an unrealistic extent, selecting a BCG on the edge of a cutout or finding a BCG from a structure at a different redshift; however, when applying our algorithm to a set of sample clusters (see Section 3.3), 92% of the selected BCGs remain unchanged from the initial guess. For those that do move, the change in redshift is normally distributed with $\sigma_{\Delta z} = 0.02$, and the median positional shift on the sky is 53 arcseconds. In all, wandering in the BCG selection algorithm does not severely impact our results.

We identify every likely galaxy in the cluster by computing the redshift of each galaxy in a pre-defined radius about the BCG. We define cluster members as any red-sequence galaxy whose photometric uncertainty combined in quadrature with a 0.03 magnitude floor brings it within 1 sigma of the BCG's redshift. That is,

$$\sigma_z = |Z(m, c) - Z(m + \sigma_{m'}, c + \sigma_{c'})| \tag{11}$$

where $Z(m, c)$ is the redshift as a function of apparent magnitude and color, and

$$\sigma_{m'} = \sqrt{\sigma_m^2 + 0.03^2}\ ; \quad \sigma_{c'} = \sqrt{\sigma_c^2 + 0.03^2} \tag{12}$$

where σ_m is the DECaLS magnitude uncertainty, and σ_c is propagated from the magnitude uncertainties.

The added 0.03 magnitude floor is used here to account for the intrinsic color scatter in the red sequence. The compositions and ages of galaxies may affect their colors in ways that are not accounted for in our model. Adding a minimum uncertainty ensures that red-sequence galaxies whose actual colors scatter them off the notional red-sequence, beyond a scatter suggested by only the photometric uncertainties, will still be counted as cluster members.

The number of cluster members is the preliminary richness value for the cluster. We then rescale the richness to account for masking in the DECaLS catalog. The catalog geometry is described by a set of pre-generated random points distributed with uniform density across the survey footprint. We count randoms in the radius of the cluster — essentially Monte-Carlo sampling the effective area — and then rescale the preliminary richness by the ratio of the expected random to the measured random counts in the area. In general, the rescaling factor is very small, with a mean of 1.003.

3.3. *Comparison to* redMaPPer *Catalog*

In order to test the efficacy of our redshift and richness algorithm, we compare it to the results of the redMaPPer SDSS DR8 cluster catalog (Rykoff et al. 2014). redMaPPer provides locations, photometric redshifts, and richnesses for over 25,000 galaxy clusters and groups, all of which are overlapped by the DECaLS footprint. While the redMaPPer algorithm was constructed for a different purpose (primarily cluster finding, and secondarily cluster characterization), and is significantly more nuanced than ours, this comparison provides an important litmus test to ensure that the majority of our results agree with those established in the most modern literature.

The redMaPPer algorithm utilizes an iterative method to determine a suitable search radius for the cluster, but our algorithm does not implement such a function.

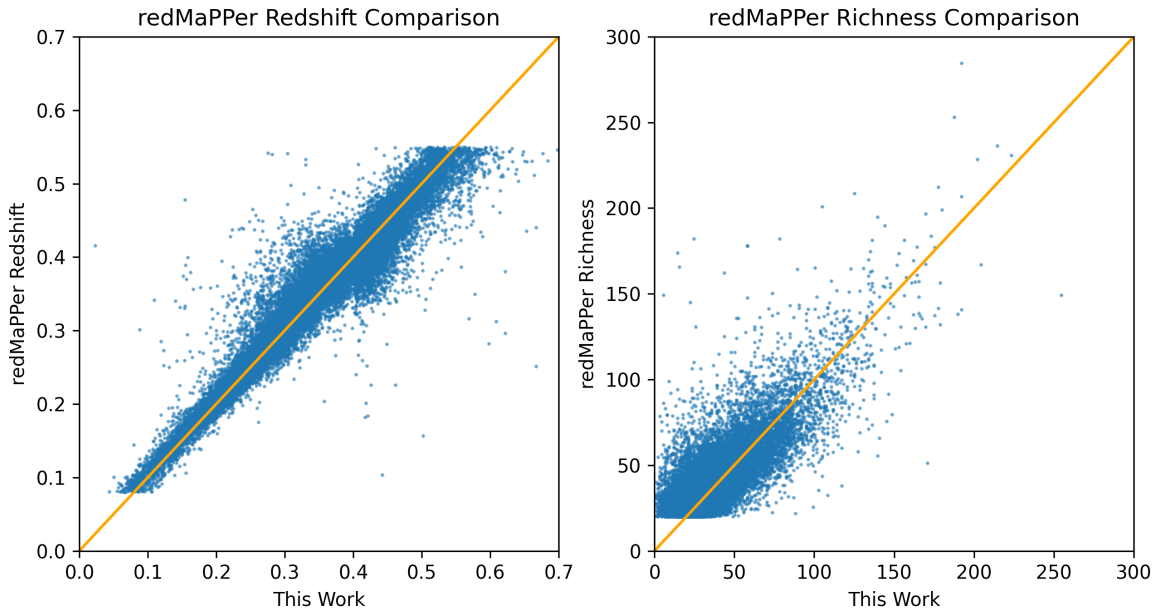

Figure 5. The redshift (left) and richness (right) for clusters in the REDMAPPER algorithm and our algorithm. Orange diagonal lines denote 1-1 linear fit lines. We obtain strong positive correlations for both metrics. The visible "kink" in the redshift plot around $z = 0.4$ corresponds to the shift in our algorithm from using $g - r$ redshift to solely $r - z$ redshift (see Section 3.1 for more details).

While our cluster radius is set to 500 kpc for our main analysis (following Bahcall 1981; Koester et al. 2007), in order to compare with the REDMAPPER sample, we extract the radius to the most distant identified cluster member in each REDMAPPER cluster and use this as the search radius for our own algorithm. Feeding our algorithm the location and radius of each REDMAPPER cluster yields the results shown in Figure 5.

Both richness and redshift exhibit strong positive correlation. The correlation coefficient for redshift is 0.947, and the correlation coefficient for richness is 0.721. Visually, it is apparent that the relationships are linear between both richness and redshift. This gives us confidence that we are able to successfully reproduce established results with our redshift and richness algorithm. It is noteworthy that, while the REDMAPPER catalog is based on SDSS DR8 data, we use DECaLS DR9 data — an entirely distinct survey with its own nuances. Despite this, we are broadly able to obtain the same results.

A final litmus test for our cluster selection and analysis is given by the results of Li et al. (2019), which utilizes simulations to model the detectability of strongly-lensing South Pole Telescope (SPT) clusters. The results are shown in Figure 6. Our redshift cumulative distribution function is closely aligned with that of Li et al. (2019). Notably, both distributions find the vast majority of lensing clusters between $0.2 < z < 1.2$. The tendency for the COOL-LAMPS sample to favor higher redshifts may be explained by the mass difference between the two samples. The SPT sample contains high mass clusters ($z_{median} = 0.55$ and median mass $M_{500} = 3.5 \times 10^{14} M_{\odot} h^{-1}$; Bleem et al. 2015), while COOL-LAMPS (being optically selected) contains significant

numbers of lower-mass systems. Since the most massive galaxy clusters are found at low redshifts, the SPT sample has a greater fraction of its catalog at low redshifts. This agreement confirms that our both our redshift algorithm and lensing cluster selection process are well-matched with modern data such as SPT.

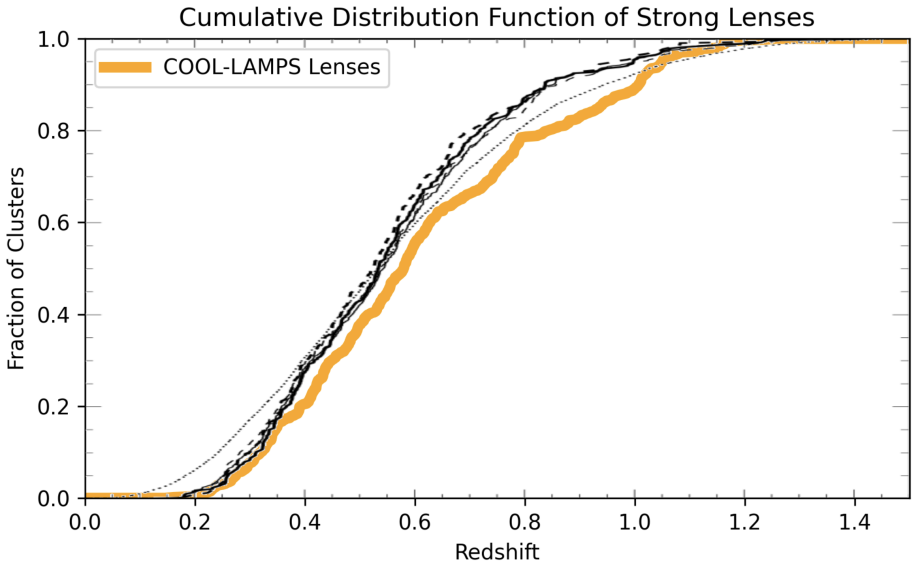

Figure 6. The redshift cumulative distribution function for our sample of lensing clusters, with model distribution functions corresponding to South Pole Telescope catalogs from Figure 3 of Li et al. (2019) overplotted. Our distribution matches these predictions remarkably well, especially at $z < 0.6$.

Because our analysis is comparative, any incompleteness in our catalog at high redshift will not bias our results. Therefore, we have not at present implemented a correction scheme for the incompleteness of the DECaLS data. We do, however, expect this incompleteness to affect our richness measurements individually, and caution against comparing high- and low-redshift clusters with the current algorithm.

3.4. *Matching Samples*

The COOL-LAMPS lensing search process begins with a set of luminous red galaxy positions. We apply our redshift and richness algorithms to each of these positions, resulting in a set of likely clusters which may be tailored further by implementing minimum richness cuts. By matching the resulting redshifts and richnesses to our known lensing cluster list, we obtain a matched set of clusters, henceforth referred to as our non-lensing cluster sample. For each lensing cluster, we select the nearest 20 non-lensing clusters in the redshift-richness space, with redshift weighted by 70 such that both parameters are on the same order of magnitude. The results are shown in Figure 7.

The resulting matched sample has a mean richness within 0.09 of the lenses, and a mean redshift within 0.001. A Kolmogorov-Smirnov test yields a 99% p-value when comparing both the two richness distributions and the two redshift distributions. There is no evidence that our matched non-lensing sample is a distinct population when compared to the richness and redshift of our lensing sample.

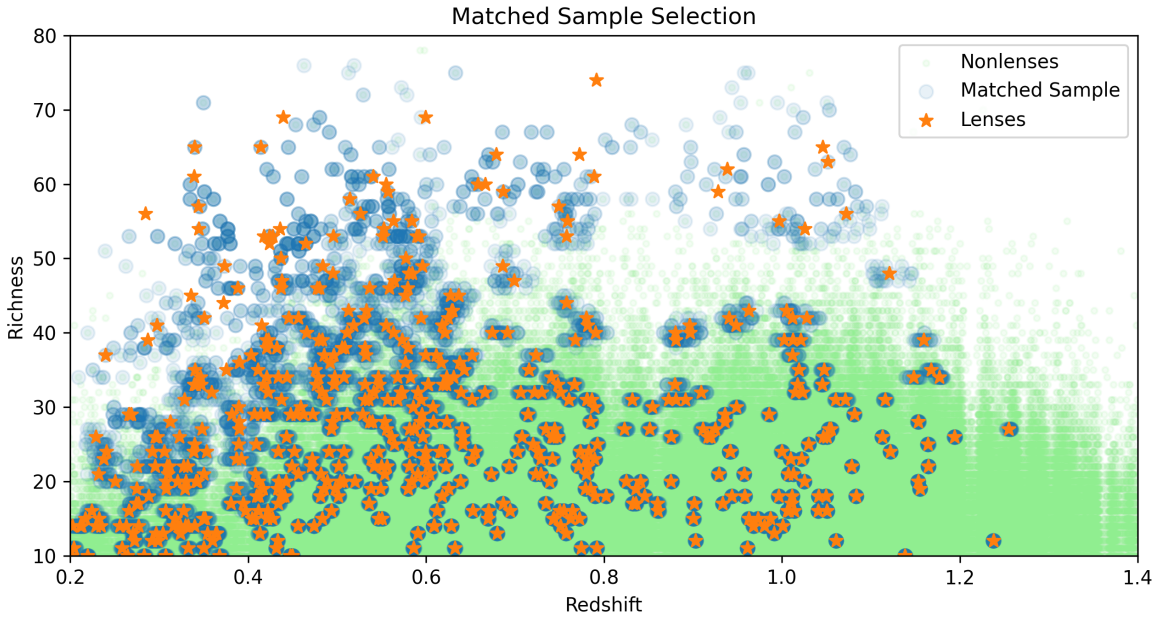

Figure 7. The redshift-richness space for the lensing and non-lensing samples. A matched non-lensing sample is selected by finding the nearest 20 non-lensing clusters to each lensing cluster. The redshift is weighted in the selection process so that redshift (with a range 0-1) and richness (with a range 0-70) have equal importance.

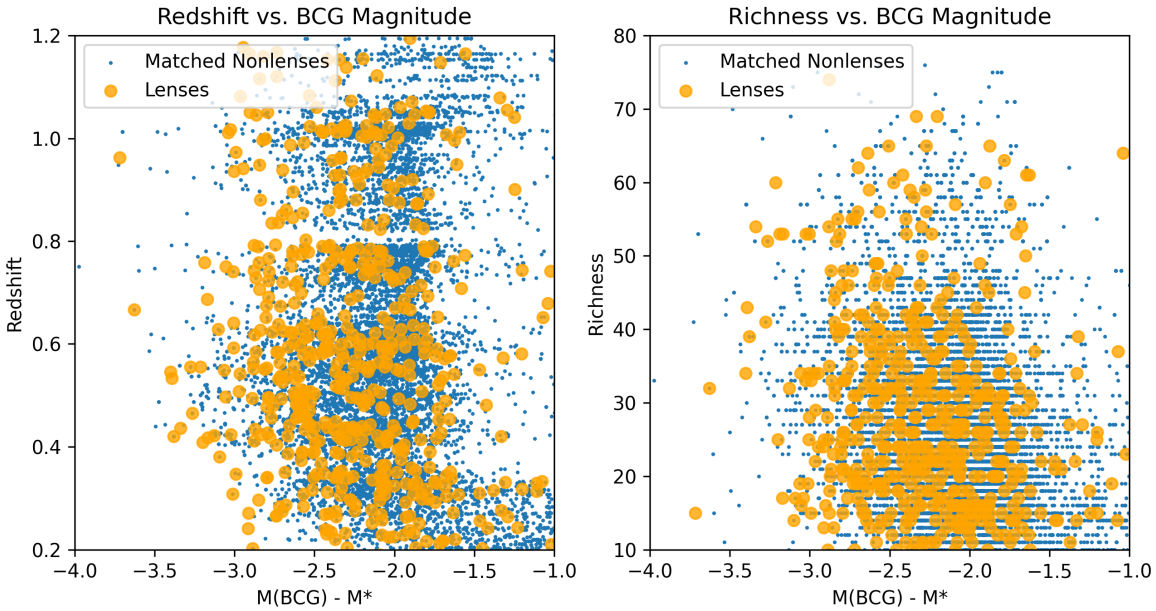

Figure 8. Left: Comparison of redshift and ΔM for matched lensing and non-lensing clusters. The trend is generally independent of redshift. Right: Comparison of richness and ΔM for matched lensing and non-lensing clusters.

4. ANALYSIS AND RESULTS

4.1. *BCG Magnitudes*

To compare the BCG luminosities of our lensing cluster sample and its matched counterparts, as motivated by Stephan (2014), we compute the $M_{BCG} - M*$ values

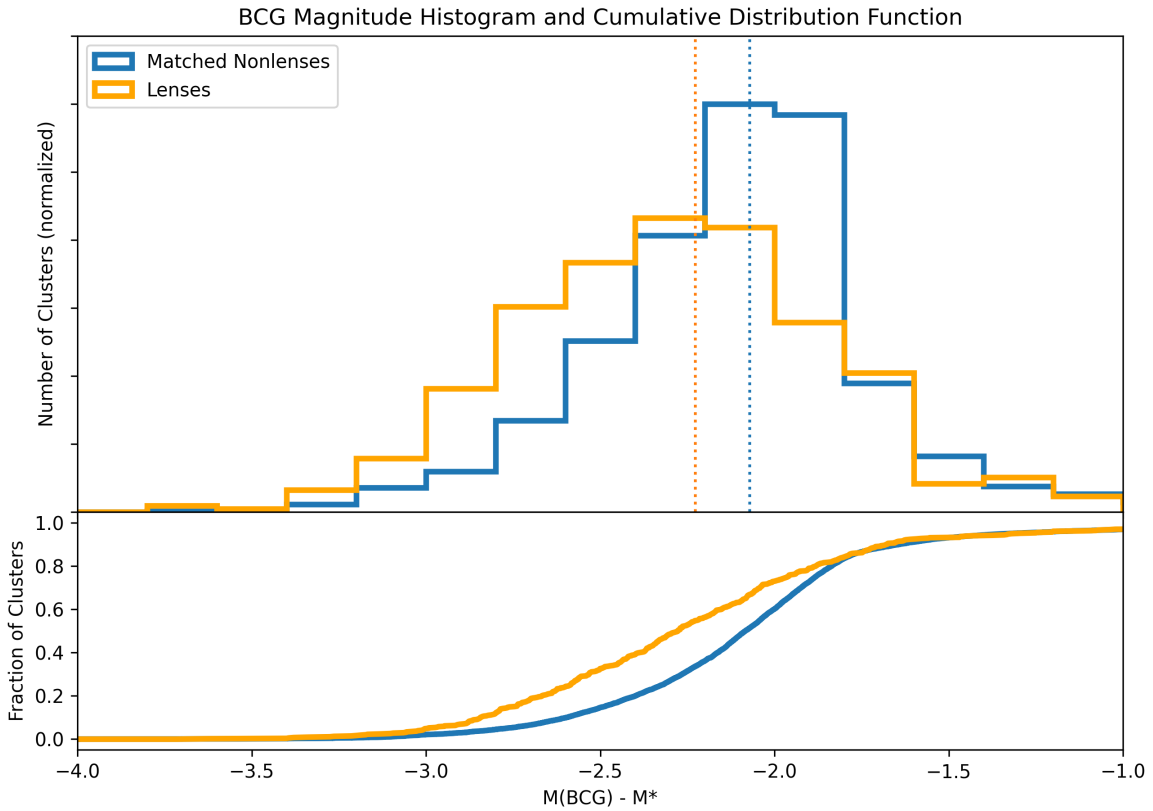

Figure 9. Top: The normalized ΔM distributions for matched lensing and non-lensing clusters. Vertical lines denote the distribution means. Bottom: Cumulative distribution functions for ΔM in matched lensing and non-lensing clusters.

(henceforth ΔM) for each. The value of M* is adapted from that described in the redMaPPer catalogs, tailored to the DECaLS filters, and extended to higher redshifts as for the overall red sequence model (see Section 3.1). In the analysis that follows, we ignore groups with richnesses below 10, as we are only interested in the properties of large, cluster-scale lensing systems. We also remove the handful of lensing clusters found at $z < 0.2$, as such clusters have less reliable photometric redshifts with g as the bluest filter; all but two of the seven lenses removed by this cut are also removed by the richness limit imposed. These cuts result in a final sample of 588 lensing systems.

In general, both lensing and non-lensing BCGs tend to be much brighter than $M*$ (Figure 9). On average, ΔM for non-lensing clusters is -2.071 ± 0.010, while for lensing clusters it is $-2.227^{+0.051}_{-0.047}$. This translates to a 15.4% increase in luminosity on average. A 2-sample T-test yields a p-value of 6.99×10^{-12}. We additionally compare the cumulative distribution functions using a Kolmogorov-Smirnov test, which yields a p-value of 2.47×10^{-22}.

The original magnitude limit used in the COOL-LAMPS search was $M * -0.5$; the fact that these BCGs are almost all well brighter than this value indicates that few cluster-scale systems are missed by executing the COOL-LAMPS lens search around LRGs rather than a predefined cluster sample. This is consistent with the observation that more than 95% of SGAS lenses are recovered by this cut.

4.2. *Additional Parameters*

While the main motivation of this study is to confirm previous observations on the luminosities of lensing BCGs, we also compare various structural parameters of the BCG and cluster in order to gain clues as to the source of the luminosity discrepancy. We compare the half-light fitted radius and ellipticity of the BCG as measured by the DECaLS Tractor algorithm (Lang et al. 2016), as well as the physical distance from the BCG to the second-brightest cluster member. The results are shown in Figure 10. Of these parameters, radius shows a significant difference, with lensing BCG radii being on average 27.0% larger than non-lensing BCG radii. A Kolmogorov-Smirnov test for radius distribution yields a p-value of 9.09×10^{-15}. There is no significant difference in ellipticity. The distance between the BCG and second-brightest member, as projected on the sky, tends to be smaller for lensing clusters, with $p = 0.031$. This marginal detection is consistent with idea that projected galaxy distribution is more compact for lensing clusters (see 4.3).

4.3. *Cluster Aperture*

We compare the density of our sample clusters by computing the richness at smaller apertures. The density is measured as the ratio between the richness at the smaller aperture and the richness at the initial aperture. Our main analysis uses 500 kpc as a hard boundary, and we perform these additional measurements using 250 kpc and 125 kpc. The results are shown in Figure 11.

We find that lensing clusters have a significantly larger ratio for both $\lambda_{250}/\lambda_{500}$ and $\lambda_{125}/\lambda_{500}$ as compared to matched non-lensing clusters. In other words, lensing clusters have a greater fraction of their galaxies concentrated within 250 kpc and 125 kpc than non-lensing clusters. A Kolmogorov-Smirnov test yields a p-value below 10^{-75} for both $\lambda_{250}/\lambda_{500}$ and $\lambda_{125}/\lambda_{500}$. Quantitatively, $44.1\% \pm 0.009\%$ of lensing cluster galaxies are contained within 250 kpc of the BCG on average, compared to only $27.6\% \pm 0.004\%$ for non-lensing cluster galaxies.

Matching the lensing and non-lensing samples using a smaller aperture for richness does not significantly affect the other measurements in this study. This makes sense, as the majority of our parameters are properties of the BCG, which does not change with aperture. For example, Figure 12 demonstrates that the differences in the ΔM distribution between the three apertures is far less than the difference with respect to the lensing sample. Matching at any of the three radii produces the same result: that BCGs are more luminous in lensing systems compared to non-lensing systems.

5. DISCUSSION

We find evidence that lensing BCGs are significantly brighter than non-lensing BCGs when compared to a characteristic magnitude $M*$. On average, we find that lensing BCGs are 15.4% more luminous than their non-lensing counterparts. This difference is statistically significant, with $p_{\text{T-test}}$ and $p_{\text{KS-test}}$ both below 10^{-11}. We

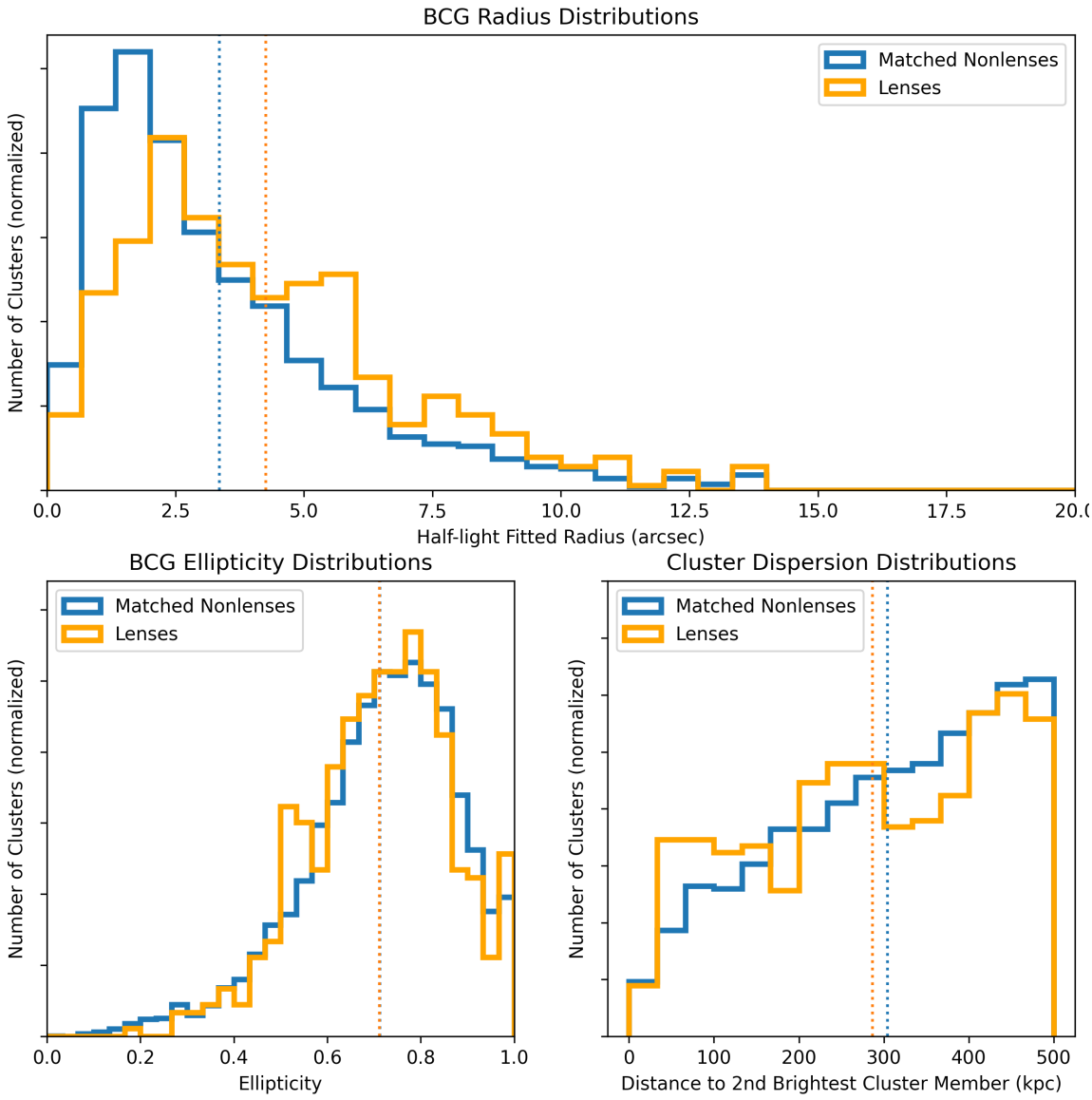

Figure 10. The normalized distributions for half-light radius (top), ellipticity (bottom left), and distance to second brightest cluster member (bottom right), for matched lensing and non-lensing clusters. Vertical lines denote the distribution means.

conclude that lensing and non-lensing cluster BCGs are highly unlikely to have the same population luminosity distribution.

These results agree broadly with the findings of previous work. Stephan (2014) computes an average luminosity difference of 61.0% , with an average lensing $\Delta M = -1.74 \pm 0.11$ and non-lensing $\Delta M = -1.22 \pm 0.01$. In comparison, our results show a smaller average luminosity difference and brighter BCGs for both the lensing and non-lensing samples. These differences may be explained by the fact that Stephan (2014) uses non-DECaLS data, a different $M*$ model, and only 10% of the lensing sample size used here. In addition, Kravtsov et al. (2018) and others have suggested that luminosity measurements in SDSS data may be underestimated, especially in

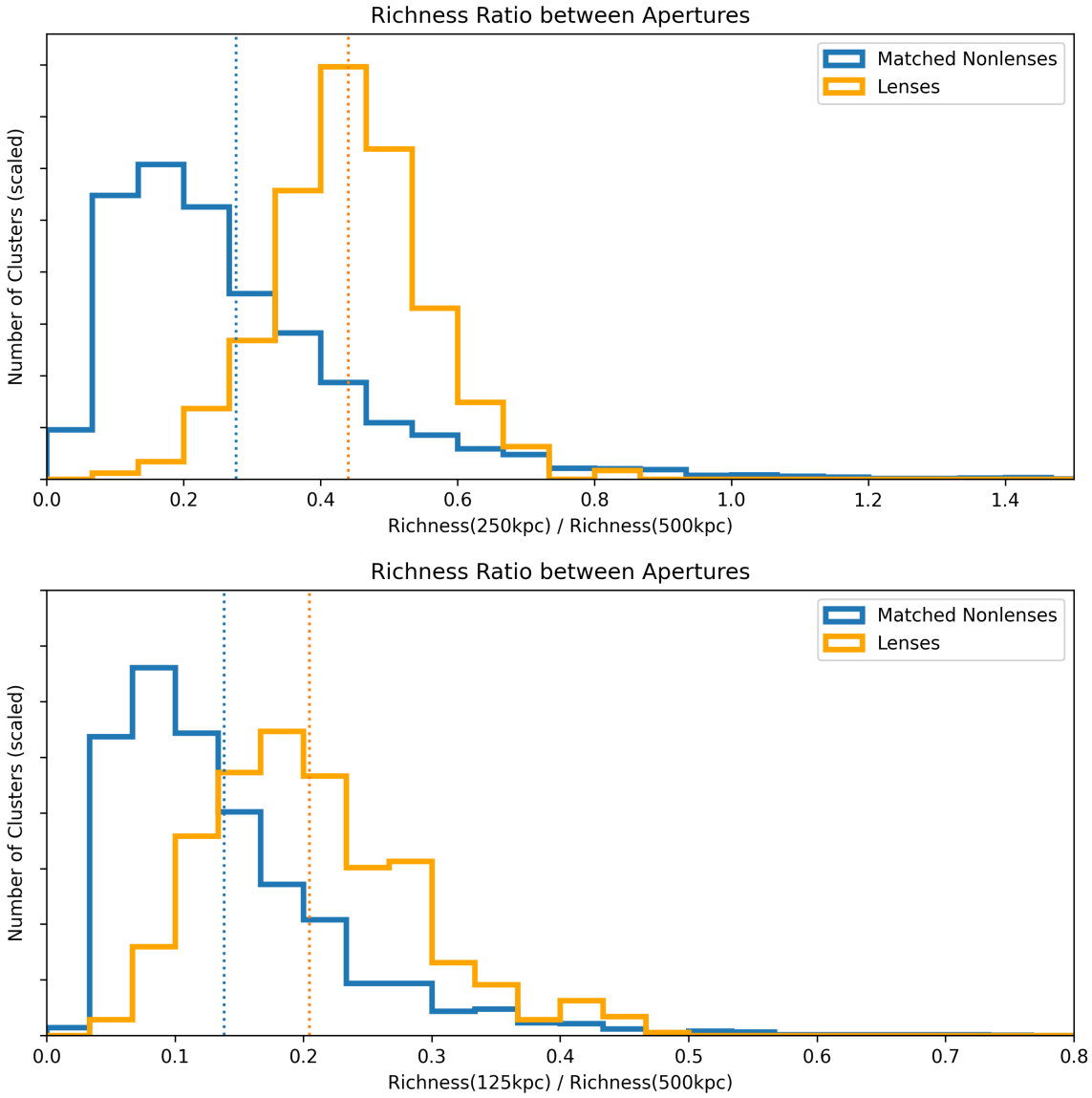

Figure 11. The ratio between richness counts for various cluster apertures (measured in kpc) for matched lensing and non-lensing clusters. Vertical lines denote the distribution means. Top: $\lambda_{250}/\lambda_{500}$. Bottom: $\lambda_{125}/\lambda_{500}$.

large galaxies such as BCGs. The noted challenge in BCG photometry in the SDSS is in capturing the low surface brightness light at large radii, and we anticipate that the model-fitting photometry of the Tractor pipeline used in DECaLS probably captures this light more robustly. Since Stephan (2014) relied on SDSS data to select clusters and measure galaxy properties, this issue would present yet another confounding factor. Nonetheless, the discrepancy is worth additional study.

The BCG luminosity relation (Figure 8) does not display significant dependence on redshift, but there is a suggestion of a slight redshift discrepancy. The average difference in ΔM between lensing and non-lensing clusters at $z < 0.7$ is -0.138 ± 0.057, while for $z > 0.7$ clusters it is -0.212 ± 0.078. These intervals slightly overlap. However, follow-up data may reveal a true pattern here. A redshift dependence in

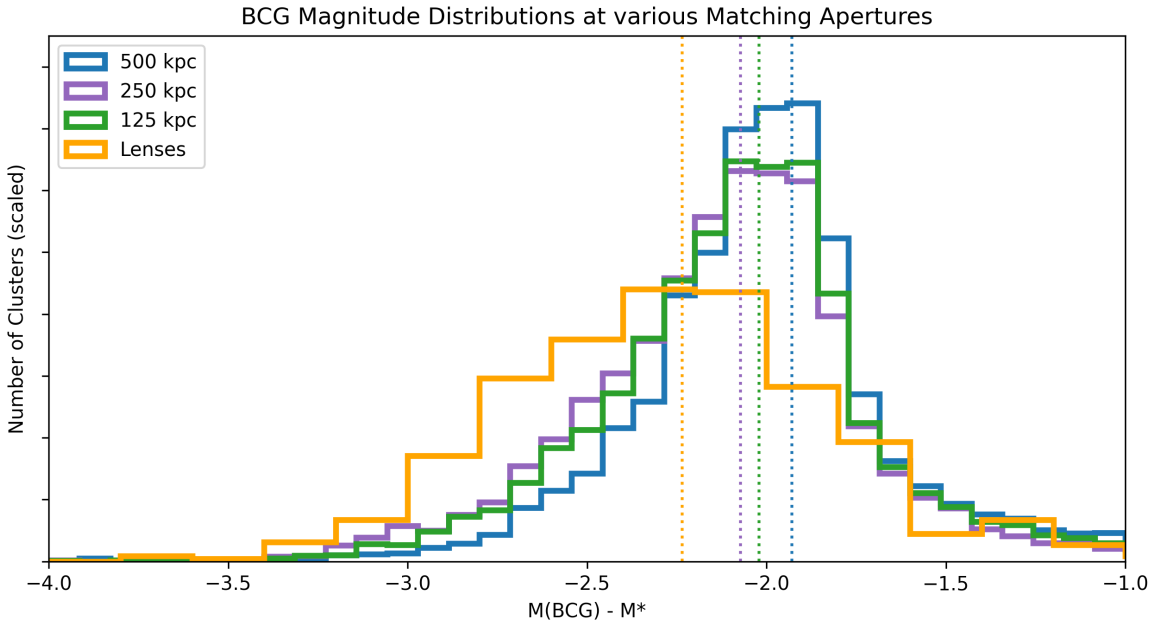

Figure 12. The ΔM distributions for non-lensing clusters matched using richness at 500 kpc, 250 kpc, and 125 kpc. The distributions do not differ beyond small statistical fluctuations.

Table 1. Study Data and Significance Values

Parameter	Lensing Mean	Non-Lensing Mean	$p_{\text{KS-test}}$	$p_{\text{T-test}}$
ΔM	$-2.227^{+0.052}_{-0.048}$	-2.071 ± 0.010	2.47×10^{-22}	6.99×10^{-12}
BCG Radius (arcsec)	4.256 ± 0.224	3.352 ± 0.049	9.09×10^{-15}	—
Ellipticity	0.711 ± 0.013	0.712 ± 0.003	0.193	0.880
Distance to 2nd Brightest (kpc)	$286.62^{+11.292}_{-12.379}$	$304.558^{+2.472}_{-2.497}$	0.031	—
$\lambda_{250}/\lambda_{500}$	0.441 ± 0.009	0.276 ± 0.004	2.24×10^{-160}	—
$\lambda_{125}/\lambda_{500}$	0.205 ± 0.007	0.138 ± 0.002	4.48×10^{-76}	—

Note—2-sample T-test results are noted where applicable (only for gaussian-appearing distributions).

ΔM may indicate the existence of a BCG property which affects luminosity and is established early on in cluster formation, and is then diluted at lower redshifts by the evolution of the cluster (through mergers, for example) or by having other clusters, which would not have appeared as lenses at high redshifts, join the lower redshift lens sample.

We further find evidence that lensing BCGs are significantly larger than non-lensing BCGs, having a 27.0% larger radius on average. This trend, combined with the luminosity disparity, supports the hypothesis that the stellar mass of lensing BCGs is greater than non-lensing BCGs, even in richness-matched clusters; as massive galaxies tend to be both brighter and larger than less-massive counterparts (Vale & Ostriker 2004).

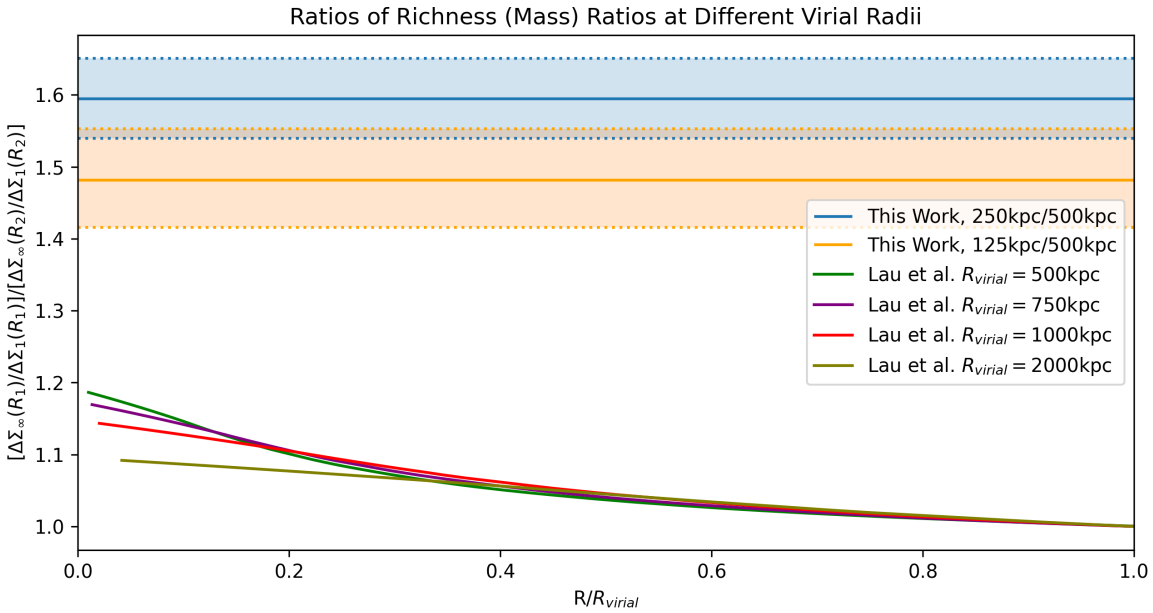

Figure 13. Comparison of $\Delta\Sigma_\infty/\Delta\Sigma_1$ ratio distributions for this work and Lau et al. (2021). Horizontal shaded regions denote the mean values and 95% confidence intervals for this work when comparing the ratios of lensing and non-lensing clusters. Additional lines represent Lau et al. (2021) predictions for $\Delta\Sigma_\infty/\Delta\Sigma_1$ ratios across radii, with R normalized to R_{virial}, and R_{virial} set to various values between 500 kpc and 2000kpc.

We additionally find that lensing clusters are significantly denser along the line-of-sight than non-lensing clusters, with $p_{\text{KS-test}}$ both below 10^{-75}. This result makes intuitive sense, as the mass distribution of clusters is directly related to the lensing cross section. Dark matter halos, and by extension the baryonic matter within them, are not perfectly spherical; they are well-described by a triaxial ellipsoid shape (Jing & Suto 2002). A cluster that is oriented with its longest axis along the lensing line-of-sight, therefore, will appear to be denser within a given aperture when compared to a cluster of the same richness that is oriented with its longest axis perpendicular to the lensing line-of-sight. Such an orientation bias has been previously noted for lensing clusters (e.g., Groener & Goldberg 2014; Lau et al. 2021).

In order to test whether this is a potential explanation for our data, we use the results of Lau et al. (2021), who model the surface mass density profiles ($\Delta\Sigma_\gamma$) for simulated clusters sampled at at various orientations to the observer (where $\gamma = 1$ signifies random mass alignment and $\gamma = \infty$ signifies maximum alignment). Under the assumption that the galaxy distributions trace underlying mass — an assumption that has been applied to model cluster-scale lenses (e.g., Sebesta et al. 2016) — we may use the results of Lau et al. (2021) to test whether orientation bias is sufficient to explain the observed data.

Given that galaxy distributions trace mass density, cluster richness is analogous to $\Delta\Sigma$ for our clusters. We use $\gamma = \infty$ to set an upper bound for the maximum orientation bias in lensing clusters. Conversely, $\gamma = 1$ represents the expected random orientation of all clusters on the sky, corresponding to our non-lensing sample. We then have the equation:

$$\frac{\lambda_{lens}(R_1)/\lambda_{lens}(R_2)}{\lambda_{non-lens}(R_1)/\lambda_{non-lens}(R_2)} = \frac{\int_0^{R_1} \Delta\Sigma_\infty(r)dr / \int_0^{R_2} \Delta\Sigma_\infty(r)dr}{\int_0^{R_1} \Delta\Sigma_1(r)dr / \int_0^{R_2} \Delta\Sigma_1(r)dr} \tag{13}$$

which allows for direct comparison between our data and that of Lau et al. (2021). This comparison is shown in Figure 13. We plot the model $\Delta\Sigma_\infty/\Delta\Sigma_1$ ratios across a variety of virial radii ranging from 500 kpc to 2000 kpc, as well as the $\Delta\Sigma_\infty/\Delta\Sigma_1$ ratios of our data. There is no point within the virial radius at which these values overlap, suggesting that orientation bias alone cannot account for the differing lensing and non-lensing richness ratios at different apertures.

Interestingly, we see marginal evidence for an inversion of these values in that the ratio for $\lambda_{125}/\lambda_{500}$ is smaller than that for $\lambda_{250}/\lambda_{500}$, where as the results of Lau et al. (2021) predict a value always rising to the center. This difference is possibly due to a core in the galaxy count distribution, which we suspect would disappear if one examined the radial distribution of cluster galaxy light as opposed to cluster galaxy counts.

6. CONCLUSION AND FUTURE WORK

We analyze a sample of 588 strongly-lensing brightest cluster galaxies between $0.2 < z < 1.2$ using a custom photometric redshift and richness estimation algorithm. We compare our lensing sample to an extensive set of non-lensing clusters that are matched to the lenses in both richness and redshift. We confirm previous findings that lensing BCGs are more luminous than non-lensing counterparts with $p < 10^{-11}$, and quantify the magnitude of the discrepancy as 15.4%. We additionally find that lensing BCGs have a 27.0% larger half-light radius than non-lensing counterparts with $p < 10^{-14}$, and that lensing clusters are more dense along the line-of-sight than non-lensing clusters at 250 and 125 kpc with $p < 10^{-75}$. Supporting these details is a marginally significant difference between cluster merger state (measured as the distance between the BCG and second-brightest cluster member) between lensing and non-lensing clusters. These results follow the predictions of Gladders et al. (2003), which suggest that structural elements of lensing BCGs and/or clusters are important flags for the lensing cross section. We find no evidence that ellipticity is distinct between the lensing and non-lensing cluster populations.

Much of the effort in this thesis has been devoted to developing the toolkit necessary to make the measurements described above. The comparisons between lensing and non-lensing clusters that we have detailed are by no means an exhaustive exploration of this topic, and we expect that future work will take advantage of our toolkit to explore these questions further across multiple projects.

ACKNOWLEDGMENTS

I am deeply grateful to my thesis advisor, Professor Michael Gladders, for his mentorship and guidance throughout this project.

This work is supported by The College Undergraduate program at the University of Chicago, and the Department of Astronomy and Astrophysics at the University of Chicago.

The Legacy Surveys consist of three individual and complementary projects: the Dark Energy Camera Legacy Survey (DECaLS; Proposal ID #2014B-0404; PIs: David Schlegel

and Arjun Dey), the Beijing-Arizona Sky Survey (BASS; NOAO Prop. ID #2015A-0801; PIs: Zhou Xu and Xiaohui Fan), and the Mayall z-band Legacy Survey (MzLS; Prop. ID #2016A-0453; PI: Arjun Dey). DECaLS, BASS and MzLS together include data obtained, respectively, at the Blanco telescope, Cerro Tololo Inter-American Observatory, NSF's NOIRLab; the Bok telescope, Steward Observatory, University of Arizona; and the Mayall telescope, Kitt Peak National Observatory, NOIRLab. The Legacy Surveys project is honored to be permitted to conduct astronomical research on Iolkam Du'ag (Kitt Peak), a mountain with particular significance to the Tohono O'odham Nation.

NOIRLab is operated by the Association of Universities for Research in Astronomy (AURA) under a cooperative agreement with the National Science Foundation.

This project used data obtained with the Dark Energy Camera (DECam), which was constructed by the Dark Energy Survey (DES) collaboration. Funding for the DES Projects has been provided by the U.S. Department of Energy, the U.S. National Science Foundation, the Ministry of Science and Education of Spain, the Science and Technology Facilities Council of the United Kingdom, the Higher Education Funding Council for England, the National Center for Supercomputing Applications at the University of Illinois at Urbana-Champaign, the Kavli Institute of Cosmological Physics at the University of Chicago, Center for Cosmology and Astro-Particle Physics at the Ohio State University, the Mitchell Institute for Fundamental Physics and Astronomy at Texas A&M University, Financiadora de Estudos e Projetos, Fundacao Carlos Chagas Filho de Amparo, Financiadora de Estudos e Projetos, Fundacao Carlos Chagas Filho de Amparo a Pesquisa do Estado do Rio de Janeiro, Conselho Nacional de Desenvolvimento Cientifico e Tecnologico and the Ministerio da Ciencia, Tecnologia e Inovacao, the Deutsche Forschungsgemeinschaft and the Collaborating Institutions in the Dark Energy Survey. The Collaborating Institutions are Argonne National Laboratory, the University of California at Santa Cruz, the University of Cambridge, Centro de Investigaciones Energeticas, Medioambientales y Tecnologicas-Madrid, the University of Chicago, University College London, the DES-Brazil Consortium, the University of Edinburgh, the Eidgenossische Technische Hochschule (ETH) Zurich, Fermi National Accelerator Laboratory, the University of Illinois at Urbana-Champaign, the Institut de Ciencies de l'Espai (IEEC/CSIC), the Institut de Fisica d'Altes Energies, Lawrence Berkeley National Laboratory, the Ludwig Maximilians Universitat Munchen and the associated Excellence Cluster Universe, the University of Michigan, NSF's NOIRLab, the University of Nottingham, the Ohio State University, the University of Pennsylvania, the University of Portsmouth, SLAC National Accelerator Laboratory, Stanford University, the University of Sussex, and Texas A&M University.

BASS is a key project of the Telescope Access Program (TAP), which has been funded by the National Astronomical Observatories of China, the Chinese Academy of Sciences (the Strategic Priority Research Program "The Emergence of Cosmological Structures" Grant # XDB09000000), and the Special Fund for Astronomy from the Ministry of Finance. The BASS is also supported by the External Cooperation Program of Chinese Academy of Sciences (Grant # 114A11KYSB20160057), and Chinese National Natural Science Foundation (Grant # 11433005).

The Legacy Survey team makes use of data products from the Near-Earth Object Wide-field Infrared Survey Explorer (NEOWISE), which is a project of the Jet Propulsion Laboratory/California Institute of Technology. NEOWISE is funded by the National Aeronautics and Space Administration.

The Legacy Surveys imaging of the DESI footprint is supported by the Director, Office of Science, Office of High Energy Physics of the U.S. Department of Energy under Contract No. DE-AC02-05CH1123, by the National Energy Research Scientific Computing Center, a DOE Office of Science User Facility under the same contract; and by the U.S. National Science Foundation, Division of Astronomical Sciences under Contract No. AST-0950945 to NOAO.

The Photometric Redshifts for the Legacy Surveys (PRLS) catalog used in this paper was produced thanks to funding from the U.S. Department of Energy Office of Science, Office of High Energy Physics via grant DE-SC0007914.

Funding for the Sloan Digital Sky Survey IV has been provided by the Alfred P. Sloan Foundation, the U.S. Department of Energy Office of Science, and the Participating Institutions.

SDSS-IV acknowledges support and resources from the Center for High Performance Computing at the University of Utah. The SDSS website is www.sdss.org.

SDSS-IV is managed by the Astrophysical Research Consortium for the Participating Institutions of the SDSS Collaboration including the Brazilian Participation Group, the Carnegie Institution for Science, Carnegie Mellon University, Center for Astrophysics — Harvard & Smithsonian, the Chilean Participation Group, the French Participation Group, Instituto de Astrofísica de Canarias, The Johns Hopkins University, Kavli Institute for the Physics and Mathematics of the Universe (IPMU) / University of Tokyo, the Korean Participation Group, Lawrence Berkeley National Laboratory, Leibniz Institut für Astrophysik Potsdam (AIP), Max-Planck-Institut für Astronomie (MPIA Heidelberg), Max-Planck-Institut für Astrophysik (MPA Garching), Max-Planck-Institut für Extraterrestrische Physik (MPE), National Astronomical Observatories of China, New Mexico State University, New York University, University of Notre Dame, Observatário Nacional / MCTI, The Ohio State University, Pennsylvania State University, Shanghai Astronomical Observatory, United Kingdom Participation Group, Universidad Nacional Autónoma de México, University of Arizona, University of Colorado Boulder, University of Oxford, University of Portsmouth, University of Utah, University of Virginia, University of Washington, University of Wisconsin, Vanderbilt University, and Yale University.

Software: `Matplotlib (Hunter 2007), Numpy (Harris et al. 2020), Scipy (Virtanen et al. 2020), Astropy (Astropy Collaboration et al. 2013, 2018), Jupyter, IPython Notebooks, SAO Image DS9 (Joye & Mandel 2003)`

REFERENCES

Abell, G. O. 1958, ApJS, 3, 211, doi: 10.1086/190036

Abell, G. O., Corwin, Harold G., J., & Olowin, R. P. 1989, ApJS, 70, 1, doi: 10.1086/191333

Astropy Collaboration, Robitaille, T. P., Tollerud, E. J., et al. 2013, A&A, 558, A33, doi: 10.1051/0004-6361/201322068

Astropy Collaboration, Price-Whelan, A. M., Sipőcz, B. M., et al. 2018, AJ, 156, 123, doi: 10.3847/1538-3881/aabc4f

Bahcall, N. A. 1981, ApJ, 247, 787, doi: 10.1086/159090

Bartelmann, M., Huss, A., Colberg, J. M., Jenkins, A., & Pearce, F. R. 1998, A&A, 330, 1. https://arxiv.org/abs/astro-ph/9707167

Baum, W. A. 1959, PASP, 71, 106, doi: 10.1086/127346

Blanton, M. R., Bershady, M. A., Abolfathi, B., et al. 2017, AJ, 154, 28, doi: 10.3847/1538-3881/aa7567

Bleem, L. E., Stalder, B., de Haan, T., et al. 2015, ApJS, 216, 27, doi: 10.1088/0067-0049/216/2/27

Bocquet, S., Dietrich, J. P., Schrabback, T., et al. 2019, ApJ, 878, 55, doi: 10.3847/1538-4357/ab1f10

Bower, R. G., Lucey, J. R., & Ellis, R. S. 1992, MNRAS, 254, 601, doi: 10.1093/mnras/254.4.601

de Vaucouleurs, G. 1948, Annales d'Astrophysique, 11, 247

Dey, A., Schlegel, D. J., Lang, D., et al. 2019, AJ, 157, 168, doi: 10.3847/1538-3881/ab089d

Dubinski, J. 1998, ApJ, 502, 141, doi: 10.1086/305901

Gladders, M. D., Hoekstra, H., Yee, H. K. C., Hall, P. B., & Barrientos, L. F. 2003, ApJ, 593, 48, doi: 10.1086/376518

Gladders, M. D., & Yee, H. K. C. 2000, AJ, 120, 2148, doi: 10.1086/301557

Groener, A. M., & Goldberg, D. M. 2014, ApJ, 795, 153, doi: 10.1088/0004-637X/795/2/153

Harris, C. R., Millman, K. J., van der Walt, S. J., et al. 2020, Nature, 585, 357, doi: 10.1038/s41586-020-2649-2

Hartle, J. B. 2003, Gravity : an Introduction to Einstein's General Relativity (Pearson)

Hennawi, J. F., Gladders, M. D., Oguri, M., et al. 2008, AJ, 135, 664, doi: 10.1088/0004-6256/135/2/664

Huang, X., Storfer, C., Ravi, V., et al. 2020, ApJ, 894, 78, doi: 10.3847/1538-4357/ab7ffb

Hunter, J. D. 2007, Computing in Science & Engineering, 9, 90, doi: 10.1109/MCSE.2007.55

Jing, Y. P., & Suto, Y. 2002, ApJ, 574, 538, doi: 10.1086/341065

Joye, W. A., & Mandel, E. 2003, in Astronomical Society of the Pacific Conference Series, Vol. 295, Astronomical Data Analysis Software and Systems XII, ed. H. E. Payne, R. I. Jedrzejewski, & R. N. Hook, 489

Khullar, G., Gozman, K., Lin, J. J., et al. 2021, ApJ, 906, 107, doi: 10.3847/1538-4357/abcb86

Koester, B. P., McKay, T. A., Annis, J., et al. 2007, ApJ, 660, 239, doi: 10.1086/509599

Kravtsov, A. V., Vikhlinin, A. A., & Meshcheryakov, A. V. 2018, Astronomy Letters, 44, 8, doi: 10.1134/S1063773717120015

Lang, D., Hogg, D. W., & Mykytyn, D. 2016, The Tractor: Probabilistic astronomical source detection and measurement, Astrophysics Source Code Library, record ascl:1604.008. http://ascl.net/1604.008

Lau, E. T., Hearin, A. P., Nagai, D., & Cappelluti, N. 2021, MNRAS, 500, 1029, doi: 10.1093/mnras/staa3313

Li, N., Gladders, M. D., Heitmann, K., et al. 2019, ApJ, 878, 122, doi: 10.3847/1538-4357/ab1f74

Meneghetti, M., Bartelmann, M., Dahle, H., & Limousin, M. 2013, SSRv, 177, 31, doi: 10.1007/s11214-013-9981-x

Meneghetti, M., Fedeli, C., Zitrin, A., et al. 2011, A&A, 530, A17, doi: 10.1051/0004-6361/201016040

Meneghetti, M., Davoli, G., Bergamini, P., et al. 2020, Science, 369, 1347, doi: 10.1126/science.aax5164

Rykoff, E. S., Rozo, E., Busha, M. T., et al. 2014, The Astrophysical Journal, 785, 104, doi: 10.1088/0004-637x/785/2/104

Schlegel, D., Dey, A., Herrera, D., et al. 2021, in American Astronomical Society Meeting Abstracts, Vol. 53, American Astronomical Society Meeting Abstracts, 235.03

Schuecker, P., Böhringer, H., Guzzo, L., et al. 2001, A&A, 368, 86, doi: 10.1051/0004-6361:20000542

Sebesta, K., Williams, L. L. R., Mohammed, I., Saha, P., & Liesenborgs, J. 2016, MNRAS, 461, 2126, doi: 10.1093/mnras/stw1433

Stephan, A. P. 2014, B.A. Thesis

Vale, A., & Ostriker, J. P. 2004, Monthly Notices of the Royal Astronomical Society, 353, 189, doi: 10.1111/j.1365-2966.2004.08059.x

Valentinuzzi, T., Poggianti, B. M., Fasano, G., et al. 2011, A&A, 536, A34, doi: 10.1051/0004-6361/201117522

Virtanen, P., Gommers, R., Oliphant, T. E., et al. 2020, Nature Methods, 17, 261, doi: 10.1038/s41592-019-0686-2

Yee, H. K. C., & López-Cruz, O. 1999, The Astronomical Journal, 117, 1985, doi: 10.1086/300837

York, D. G., Adelman, J., Anderson, John E., J., et al. 2000, AJ, 120, 1579, doi: 10.1086/301513

Zhou, R., Newman, J. A., Mao, Y.-Y., et al. 2021, MNRAS, 501, 3309, doi: 10.1093/mnras/staa3764